Generation of topological spin textures using light-induced radially polarized magnetic field

Yunqing Jiang,[1,2,3] Pierre Vallobra,[1,3,*] Xiaoqiang Zhang,[1,3,†] Yong Xu,[1,2,3] Qiwen Zhan,[4] and Weisheng Zhao[1,2,3]

[1] *National Key Lab of Spintronics, Institute of International Innovation, Beihang University, Yuhang District, Hangzhou, 311115, China*

[2] *MIIT Key Laboratory of Spintronics, School of Integrated Circuit Science and Engineering, Beihang University, Beijing 100191, China*

[3] *Hefei Innovation Research Institute, Beihang University, Hefei 230013, China*

[4] *School of Optical-Electrical and Computer Engineering, University of Shanghai for Science and Technology, Shanghai 200093, China*

(Received 24 October 2023; revised 28 February 2024; accepted 29 March 2024; published 22 April 2024)

Laser-driven manipulation of magnetic skyrmions holds great promise for the development of next-generation information memory devices due to the flexibility of optical modulation. In this study, we theoretically present an approach for generating and manipulating stable topological spin textures using a light-induced radially polarized magnetic field, along with the ability to easily control quasiparticles by adjusting the intensity of the input beam. The generated topological spin textures can shrink into a stabilized quasiparticle with a size significantly smaller than the light-induced radially polarized magnetic field in few picoseconds. Through exploiting the relaxation mechanism of the spin texture at the center of the beam, we demonstrate the creation and stabilization of quasiparticles with higher ring numbers. Furthermore, we investigate the motion of these distinct quasiparticles and discover that the $n\pi$ quasiparticles ($n > 1$) exhibit significantly faster velocities than a traditional skyrmion, with the 4π quasiparticle being the fastest. Our method offers a promising avenue for constructing various topological spin textures with multiring profiles in ultrafast and high-density data-storage devices.

DOI: 10.1103/PhysRevApplied.21.044041

I. INTRODUCTION

To increase memory capacity, the size of individual domains for encoding an information disk needs to be reduced [1]. The robust vortexlike spin texture of topological magnetic skyrmions makes them attractive as information carriers in next-generation devices [2,3], because of its nanoscale dimensions and long-term thermal stability. Integrating computation with data storage has led the push toward exploring skyrmionic devices with higher density recording and faster manipulation, such as more than 1 Tbit/inch^2 and 60 m/s, respectively [1,3,4]. In terms of ultrafast manipulation, researchers are actively exploring alternative methods for controlling the magnetization of a medium beyond traditional magnetic fields. Electrical control of magnetization dynamics is one of those efficient methods [5,6]. Current-driven switching of topological magnetic textures, however, is hampered by challenges related to high-current-density-induced thermal instability [2,7] and the unpredictability of the magnetization-switching behavior due to the slow processional motion of the core [7]. Using a laser to manipulate magnetism is a very attractive alternative approach. Ultrafast laser pulses have been applied to trigger ultrafast demagnetization [8,9], magnetization reversal [10–13], and the manipulation of topological properties on magnetic nanostructures [7,14–17], approaching timescales of picoseconds or less. Some researchers have experimentally explored ultrafast laser-induced generation and annihilation of magnetic skyrmions, highlighting their potential for faster and more-energy-efficient information technology applications [18,19]. Printing laser profiles like skyrmion multiplexes on magnets has been theoretically proposed, thanks to optical and electron vortex beams carrying intrinsic orbital angular momentum [20]. The difficulty lies in using the proper wavelength in the region of extreme ultraviolet light to generate single topological magnetic textures. There is another feasible method without the strict limitation of wavelength. Based on the inverse Faraday effect, a controllable effective magnetic field can be generated using

*Corresponding author: pierrevallobra@buaa.edu.cn
†Corresponding author: xqzhang@buaa.edu.cn

 © 2024 American Physical Society

a circularly polarized optical beam [21–23]. In addition to the noncontact and instantaneous advantages, the distribution and direction of the light field can be tailored easily by modulating the parameters of the focal optical beam, such as wavelength, intensity [24–28]. It is noteworthy that the radially polarized magnetic field (RPMF), like a Néel-type feature, can be generated by tightly focusing two counterpropagating cylindrical vector beams (CVBs) [29]. Furthermore, the method for the generation of CVBs has been studied over the years [30,31]. Thus, the RPMF induced by the inverse Faraday effect can offer intriguing possibilities for achieving faster and more precise creation of Néel-type skyrmions.

The transmission of a skyrmion, particularly during high-speed operation, faces a notable obstacle, wherein its motion under the driving current deviates from the direction of the current [32,33]. This phenomenon is known as the skyrmion Hall effect (SkHE). In addition to the risk of annihilation at the edge, the drivable length of skyrmions is limited by the width of the nanotrack [2]. To address this challenge, the antiferromagnetically exchange-coupled bilayer system is theoretically proposed to suppress the SkHE [34]. It shows that the motion shift acting on a pair of skyrmions with opposite topological charge is cancelled out. Another intriguing approach is to utilize a magnetic skyrmionium, the topological charge of which is zero ($Q = 0$), to achieve faster velocities and reduce deformation [35–37]. Recently, circularly polarized light has been theoretically proved to manipulate the topological charge of the skyrmion structure in a frustrated magnet [38]. The corresponding simulations showed that the switching of the topological charge in the system depended on both the pulse duration and the intensity of the circularly polarized light. When the polarized light with helicity is applied to the whole system, only the skyrmions with negative topological charge are affected by the light, while those with a positive topological charge remain unchanged. While the overall topological charge can be set, depending on the light helicity, this process is stochastic and does not allow for precise control of the topological charge of a single skyrmion.

Here, we use micromagnetic simulations to study the generation and manipulation of different topological spin structures in ultrathin magnetic nanostructures by a RPMF, promising high flexibility and individual control for next-generation skyrmionic devices and applications in information processing. By tuning the intensity of the input beam, where the magnitude of the induced RPMF can be changed immediately, a magnetic skyrmion, a skyrmionium, and other $n\pi$ states with multiring profiles can be generated. These generated quasiparticles possess dimensions reduced 8 times in comparison to the size of the induced RPMF after the full relaxation time. We also explore the velocity of the generated quasiparticles when they are driven by a current in a nanotrack. Our finding reveals that, upon excitation with spin-transfer torque (STT) or spin-orbit torque (SOT), the generated 4π-state quasiparticle displays the highest velocity among the generated skyrmionium and skyrmion. This approach offers prospects for high-speed and low-power-consumption skyrmionic devices in the future.

II. THEORETICAL FRAMEWORKS

Figure 1 depicts a schematic illustration of the process for generating skyrmions and other topological magnetic quasiparticles by a RPMF. As shown in Fig. 1, two counterpropagating CVBs, each possessing an electric field $\mathbf{E}_1$ and $\mathbf{E}_2$, are focused by a tightly focused 4π configuration [39]. Their polarization angles are, respectively, rotated by $\pm 45°$ from the purely radial polarization. Many methods can be applied to generate these CVBs, e.g., using a fiber

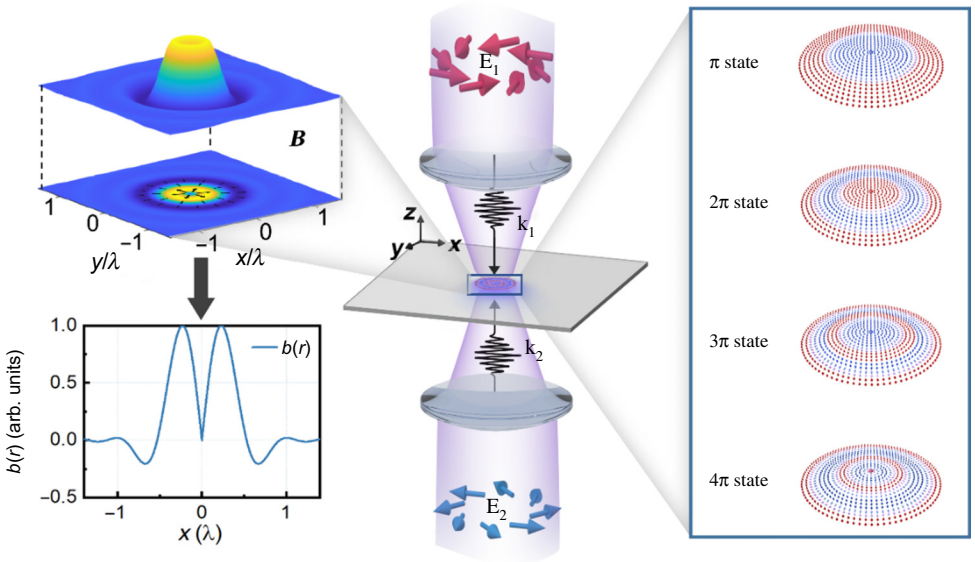

FIG. 1. Creation of topological spin textures by a RPMF. Two CVBs with electric fields $\mathbf{E}_1$ and $\mathbf{E}_2$ are tightly focused on the sample. RPMF is induced by the inverse Faraday effect (left inset). Under different amplitudes of the RPMF, four stable topological spin textures can be created (right inset).

CVB laser combined with a two-half-wave-plate polarization rotator, where the fiber CVB laser can generate a CVB with its polarization along the radial direction directly [31], and the two-half-wave-plate polarization can rotate its polarization direction by ±45°from the purely radial polarization [40]. A heterostructured thin film composed of a ferromagnetic film with magneto-optical constant χ and a heavy-metal film with a strong spin-orbit coupling is located in the confocal plane of the two lenses. Given that the thickness of the heterostructured film is on the nanometer scale, the focal shift and the reflection at the interface can be disregarded [41]. According to Richards-Wolf vector diffraction theory, the electric field in the focal region can be obtained (see Fig. S1 within the Supplemental Material [42]). As shown in Fig. S1 within the Supplemental Material [42], the radial component of the total electronic field on the focal plane is null due to the destructive interference of the two counterpropagating CVBs, while the other two components are nonzero [29]. Consequently, based on the inverse Faraday effect, a RPMF can be produced and calculated in cylindrical coordinates, as follows [26,43]:

$$\mathbf{B}_{\mathrm{RPMF}} = \mu_0 \chi (\mathbf{E} \times \mathbf{E}^{*}) = \pm B_0(r)\mathbf{e}_r, \tag{1}$$

where $\pm B_0(r) = \mu_0 \chi (E_\varphi E_z^* - E_z E_\varphi^*)$. Here, μ_0 is the vacuum permeability constant; $\mathbf{E}$ is the total electric field on the focal plane; $\mathbf{E}^*$denotes the conjugate of $\mathbf{E}$; E_φ and E_z stand for the azimuthal and longitudinal components of the total electric field at the focus, respectively; and $\mathbf{e}_r$ represents the unit vector along the radial direction. The value of B_0 is determined by the total laser pulse fluence, F, and duration, τ, of the two focused CVBs, and $B_0(r) = 2\chi F/c\tau$ [43,44]. The strength of B_0 is calculated from 0.1 to 30 T for a common laser fluence with duration from 0.1 ps to several ps [45]. For the convenience of subsequent calculations, we define $B_0(r) = I_0 b(r)$. Here, I_0 is a dimensionless value determined by the amplitude and pulse duration of the two CVBs, and $b(r)$ corresponds to the normalized radial distribution function of the induced RPMF that peaks at 1 T (as shown in the left inset of Fig. 1). In this study, $\mathbf{B}_{\mathrm{RPMF}}$ is along $-\mathbf{e}_r$ at its peak value, with the wavelength of the two input CVBs of 400 nm, the magneto-optical constant $\chi \approx 2 \times 10^{-6}$ m/A, and the pulse duration $\tau = 10$ ps. The numerical aperture (NA) of the two objective lenses is set to NA = 0.95, and this implies that the radius of the induced RPMF can be calculated to be about 200 nm [26]. We would like to point out that under other rotated angles θ of the polarization of the two CVBs (except 0, π, and $\pm\pi/2$), the total azimuthal and longitudinal components, E_φ and E_z, on the focal plane are changed. In this situation, the radial component is still zero, and a RPMF can also be induced. However, its intensity will become weaker, as shown in Fig. S2 within the Supplemental Material [42]. We can find that the induced RPMF will have the largest intensity when $\theta = \pm\pi/4$. So $\theta = \pm\pi/4$ is selected in the next simulation. To get a stable skyrmion or any other topological quasiparticle, it is claimed to be better to have a size of the induced RPMF comparable to the size of the quasiparticle in the sample [20]. As previously demonstrated in Ref. [27], the size scale of the induced magnetic field is determined by the wavelength of the focused CVBs. However, the size of a skyrmion corresponds to a local minimum of all the magnetic interactions and is consequently dictated by the magnetic parameters, among which the exchange coupling between the spins and the Dzyaloshinskii-Moriya interaction (DMI) at the interface exert a stronger influence [15,46].

To study the interplay between these effects, we conducted simulations of a thin film of 1 nm thick and in-plane dimensions of 1024×1024 nm^2. The evolution of magnetization ($\mathbf{M}$) upon the laser-induced RPMF is calculated based on the Landau-Lifshitz-Gilbert (LLG) equation [34,35]:

$$\frac{d\mathbf{M}}{dt} = -\gamma_g \mathbf{M} \times \mathbf{H}_{\mathrm{eff}} + \frac{\alpha}{M_s}\left(\mathbf{M} \times \frac{d\mathbf{M}}{dt}\right). \tag{2}$$

Here, α denotes the magnetic damping coefficient, M_s signifies the saturation magnetization, γ_g is the gyromagnetic ratio, and $\mathbf{H}_{\mathrm{eff}}$ represents the effective field. This effective field is linked to the energy density, ε, by the following relationship:

$$\mathbf{H}_{\mathrm{eff}} = \frac{1}{\mu_0}\frac{\partial \varepsilon}{\partial \mathbf{M}}. \tag{3}$$

In our study, the effective field includes the Heisenberg exchange interaction, magnetic anisotropy, DMI, dipolar field, and the light-induced RPMF contributions. The energy density can be expressed as follows:

$$\begin{aligned}\varepsilon = {} & A_{\mathrm{ex}}\left[\nabla\left(\frac{\mathbf{M}}{M_s}\right)\right]^2 - K_u\frac{(e_k \cdot \mathbf{M})^2}{{M_s}^2} - \frac{\mu_0}{2}\mathbf{M} \cdot \mathbf{H}_d(\mathbf{M}) \\ & + \frac{D}{{M_s}^2}\left(M_z\frac{\partial M_x}{\partial x} + M_z\frac{\partial M_y}{\partial y} - M_x\frac{\partial M_z}{\partial x} - M_y\frac{\partial M_z}{\partial y}\right) \\ & - \mathbf{M} \cdot \mathbf{B}_{\mathrm{RPMF}}.\end{aligned} \tag{4}$$

Here, A_{ex}, K_u, and D denote the Heisenberg exchange-energy constant, perpendicular magnetic anisotropy, and DMI energy constant, respectively. M_x, M_y, and M_z are the three components of magnetization $\mathbf{M}$. The perpendicular anisotropy unit vector and the demagnetization-field vector are represented by $\mathbf{e}_k$ and $\mathbf{H}_d(\mathbf{M})$, respectively. The material parameters utilized in this study are listed as follows: $M_s = 5 \times 10^5$ A/m, $A_{\mathrm{ex}} = 9.7 \times 10^{-12}$ J/m, $D = 3.0 \times 10^{-3}$ J/m^2, and $K_u = 0.8 \times 10^6$ J/m^3, $\alpha = 0.1$.

These parameters correspond to experimental observations for Co/Pt [47]. The calculated exchange length and helical length corresponding to these parameters are, respectively, 7.86 and 40.6 nm [48]. In comparison, our space-discretization cell has a volume of $1 \times 1 \times 1$ nm^3. The laser-pulse duration used in the simulation is 10 ps, with uniform amplitude during the pulse. The initial magnetization of the film was aligned along the $-z$ axis. The magnetization's evolution was calculated via the LLG equation, utilizing the finite-element micromagnetism software MUMAX3 [49]. Contrary to other laser studies, where the topological structures are generated due to heat [14–17,49], the focus of this work is the role of the RPMF. Thus, our study does not include heat contributions to ensure that the creation of topological structures is solely due to the RPMF.

III. RESULTS AND ANALYSIS

Depending on different values of I_0, an array of magnetic configurations can be generated, with Fig. 2 displaying the magnetization states at various times for different I_0 values. Notably, for each I_0 value, three images showcase the magnetization configuration during the pulse at 2, 6, and 10 ps, while the fourth image displays the magnetic configuration at 60 ps, i.e., 50 ps after the laser pulse's termination. Though the magnetization states at 2 ps appear similar for all I_0 values, the final (stable) states differ topologically. We ensured that a state was stable by observing that the dimensions of the quasiparticle no longer changed in 10 ps. After a standard MUMAX3 relaxing procedure on each final state [50], we confirmed that those were indeed stable.

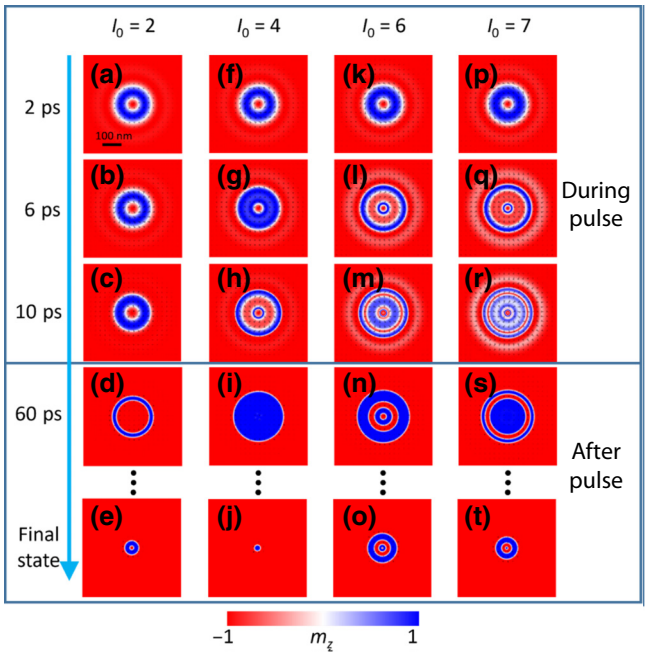

FIG. 2. Magnetization states at different times for $I_0 = 2$ (a)–(e), $I_0 = 4$ (f)–(j), $I_0 = 6$ (k)–(o), and $I_0 = 7$ (p)–(t). We define a stable state as the state where magnetization stops evolving. Time necessary to reach each stable state depends on the magnetic state generated itself.

As shown in Fig. 2, we can find that the RPMF has the capability to generate diverse topological magnetic structures, namely, $n\pi$-state quasiparticles with $n = 1$, 2, 3, and 4, where n denotes the accumulated magnetization-rotation value from the center of a quasiparticle to its edge along the radial direction. For instance, a skyrmion corresponds to a π state. Because its magnetization direction is changed from -1 to 1 when scanning from its center to its edge along the radial direction, the magnetization-rotation value is 1 [2,35]. Here, for the sake of simplicity, we refer to $n\pi$-state quasiparticles as $n\pi$ QPs. In Fig. 2, when $I_0 = 2$, 4, 6, and 7, the final states are a 2π QP (also known as a skyrmionium or doughnut [30]), π QP (skyrmion), 4π QP, and 3π QP, respectively. The formation of more rings during the laser pulse is a notable phenomenon observed for higher I_0 values. Remarkably, the final state has the same topology as the state after 60 ps for each I_0 value, with the laser creating magnetic objects of size commensurate with the beam size. After laser exposure, the magnetic texture initially stabilizes in a few hundred picoseconds and then experiences a drastic shrinkage in size during several nanoseconds, providing the possibility of creating even the smallest topological spin textures using experimentally accessible sizes of laser beams. An example of magnetic texture stabilization between the end of the pulse and 60 ps is shown in Fig. S3 within the Supplemental Material for $I_0 = 4$ [42]. It can be observed that the relaxation process is nontrivial and that, even at 50 ps, the skyrmion state is not fully homogenous, thus justifying our choice of 60 ps in Fig. 2 for a clear observation of all the quasiparticles. After stabilization, the strongest shrinkage is observed for a skyrmion with an initial diameter of 262 nm and a final diameter of 32 nm.

The dynamics during and after the pulse are dissimilar, as observed in Fig. 2. The RPMF forcefully drives the system out of equilibrium, leading to large areas of in-plane magnetization (white contrast). Conversely, after the pulse, the magnetization relaxes by forming domains with orientations along $+z$ and $-z$ due to the contribution of anisotropy. Hence, it is imperative to study magnetization evolution during and after the pulse separately. At the early stages of pulse application (2 ps), the beam center undergoes no magnetization modification, consistent with the induced RPMF reaching zero at its center. The topological charge, Q, is a critical property of $n\pi$ QPs, with Q equal to 0 (1) for even (odd) values of n because the magnetization at its center is parallel (antiparallel) to that at its edge. Ultimately, magnetization at the center can be reversed during the pulse, as indicated by the change of topological charge

observed in Fig. S4 within the Supplemental Material [42], owing to the interactions between different magnetic moments (DMI, Heisenberg exchange, and dipolar field). The creation of several rings, as observed more strikingly in Figs. 2(m) and 2(r), must be a consequence of the RPMF itself.

To gain more insight into the mechanism of formation of magnetic textures with our laser profile, we plotted the evolution of each energy during the pulse for $I_0 = 10$, as shown in Fig. 3(a). Notably, both DMI and Heisenberg exchange are included in the exchange energy plotted in Fig. 3(a). We can find the total-energy variation mainly follows the reduction of the Zeeman energy, indicating that the RPMF is the primary driving force behind the observed dynamics. To probe the distinct impact of the RPMF, we performed a simulation employing identical material parameters, but with sole interaction from the RPMF. Figure S5 within the Supplemental Material [42] shows that such a simulation also generates multiple rings during the pulse, as in our initial simulations. As time progresses, more rings are created, indicating the key role of the RPMF. Notably, the spatial distribution of the RPMF is

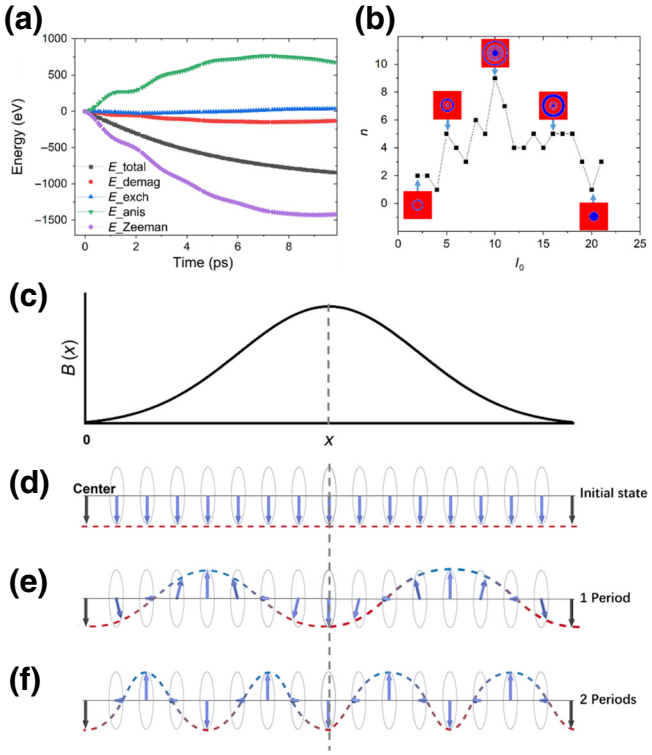

FIG. 3. Effect of the RPMF on magnetization evolution. (a) Time evolution of each energy term for $I_0 = 10$. (b) Value of n corresponding to $n\pi$ QP at 60 ps under different I_0. (c) Magnetic field with a Gaussian profile applied on the initial magnetization state (d). Resulting magnetic configurations after one precession period (e) and two precession periods (f) without damping and other interactions except for the magnetic field.

inhomogeneous, as illustrated in the left inset in Fig. 1, and is responsible for the creation of rings. We can explain the connection between inhomogeneous spatial distribution and the generation of rings by considering a Gaussian distribution of magnetic field along $-\mathbf{e}_r$, as shown in Fig. 3(c). Here, the center of magnetization is fixed at $x = 0$ of the magnetic field, and we primarily focus on the role of the precession term from the magnetic field, while temporarily ignoring the effect of damping and other interactions, except for the magnetic field. When there is no damping, a magnetic field along $-\mathbf{e}_r$ induces precession in the plane perpendicular to $-\mathbf{e}_r$, as depicted in Figs. 3(e) and 3(f). The precession period, T, is equal to $T = 2\pi/\mathbf{B}\gamma_g$, and an inhomogeneous magnetic field leads to an uneven rate of rotation. With $I_0 = 10$, this period of rotation at the peak value amounts to 3.57 ps. Starting from all magnetic moments along $-z$ [Fig. 3(d)], the configuration after 3.57 ps is displayed in Fig. 3(e). At lower magnetic field values, the magnetic moments undergo partial rotation, creating two rings with opposite magnetization. After another 3.57 ps, the magnetization at the center has performed two turns, and there are now four domains of opposite magnetization, as shown in Fig. 3(f). After each period of rotation, the number of domains with overall magnetization along $+z$ is doubled. In our actual system, the RPMF intensity plays a crucial role in the mechanism of ring formation, which is more evident when the RPMF intensity is high. Additionally, it is worth noting that the ring configuration obtained during the pulse may not be stable. This raises the possibility of ring annihilation after the pulse has ended. To investigate this phenomenon, we have plotted the cumulated magnetization (i.e., the value of n for an $n\pi$ QP) at 60 ps as a function of I_0 in Fig. 3(b). As expected from the precession effect, the value of n generally increases with the intensity of the pulse up to $I_0 = 10$, where it reaches a maximum of 9. However, upon further increasing the pulse amplitude, the value of n gradually decreases and even drops to 1 at $I_0 = 20$.

To gain further insights, we have examined the magnetization state at the end of the pulse [10 ps for $I_0 = 20$, which is shown in Fig. S6(a) within the Supplemental Material [42]]. It can be observed that the magnetization mainly has an in-plane component along $-\mathbf{e}_r$ at the location of the pulse. By removing all the interactions, except for the RPMF for $I_0 = 20$, the magnetization configuration is mostly oriented along $-\mathbf{e}_r$ [see Fig. S6(b) within the Supplemental Material [42]]. This behavior can be attributed to the damping effect, which drives the magnetization towards the direction of the applied field. When most of the magnetic moments exposed to the laser have a strong component along $-\mathbf{e}_r$ at the end of the pulse, they tend to relax more coherently, since their magnetization is more similar. Therefore, the higher the magnetic field, the more the magnetic moments align along $-\mathbf{e}_r$, which enhances the coherence of their relaxation. This explains

the observed trend of decreasing n with increasing intensity above ten, as depicted in Fig. 3(b).

Although more rings can be generated at higher amplitude values, it appears that the highest stable value of n for the $n\pi$ QP state is limited to four. Interestingly, for n greater than four, the magnetization ultimately relaxes to the 4π QP after an extended time (see Fig. S7 within the Supplemental Material [42]). Notably, the maximum stable value of n is entirely determined by the material parameters and reducing the exchange coupling to 1×10^{-11} J/m results in a reduced highest stable value of n to 3, as shown in Fig. S8 within the Supplemental Material [42]. Hence, investigating skyrmions, 2π, 3π, and 4π QPs remain most relevant for the chosen material parameters. To examine the stability of these configurations, in Figs. 4(b)–4(e) we showcase the diameter of each domain wall (DW) that separates states with opposing magnetization. In Fig. 4(a), we take the example of a 4π QP just after the end of the pulse (60 ps) to explicitly show how we define the different DWs. The first DW diameter always corresponds to the overall size of the magnetic object and, in any $n\pi$ QP, the DW with the number n corresponds to the closest DW to the center of the QP. We define the full relaxation time as the duration required for all the DWs to reach their final diameter value. As shown in Fig. 4, the associated full relaxation times are 5.8, 5.2, 11, and 12 ns, for the π, 2π, 3π, and 4π QP, respectively. While the size of an $n\pi$ QP exclusively depends on n and the material parameters, the same cannot be said for its full relaxation time. Indeed, the value of I_0 alters the magnetic state right after the pulse, thus affecting the relaxation dynamics and time. Therefore, the relaxation times presented in Fig. 4 are specific to each I_0 value, and they correspond to I_0 in Fig. 1. The overall size of the quasiparticles after full relaxation, shown in Fig. 4, is far smaller than the wavelength of the laser. This method could be particularly attractive as an alternative way to generate skyrmions due to its wider and more feasible selection of wavelengths.

The excited robust vortexlike spin texture might become an information carrier in next-generation spintronic devices only if it can be easily moved at lower energy costs. To evaluate the comparative effectiveness of various magnetic quasiparticles generated by the RPMF, we sought to determine their respective velocities when

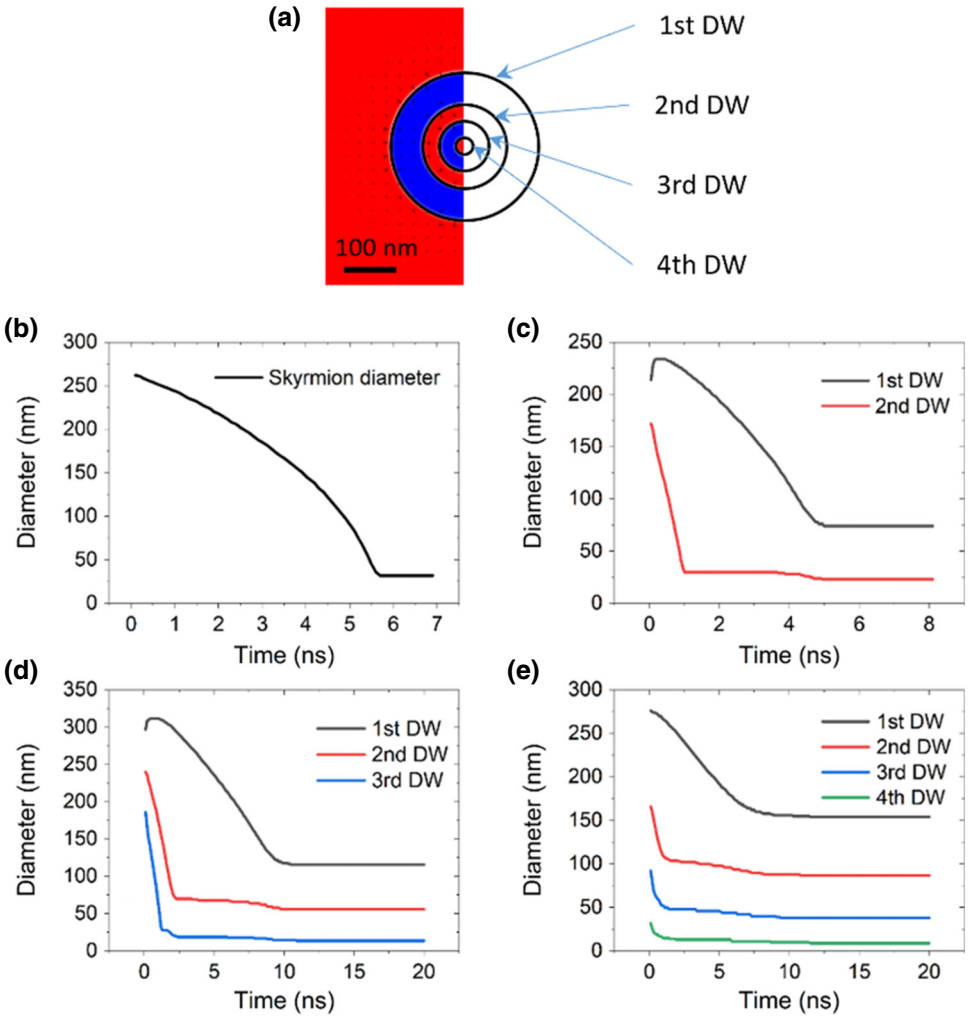

FIG. 4. Shrinking process of $n\pi$ QPs after the pulse. (a) Scheme of different numbers of DWs in a 4π QP. Evolution of the distance between each domain wall and the center for a skyrmion (b), 2π QP (c), 3π QP (d), and 4π QP (e).

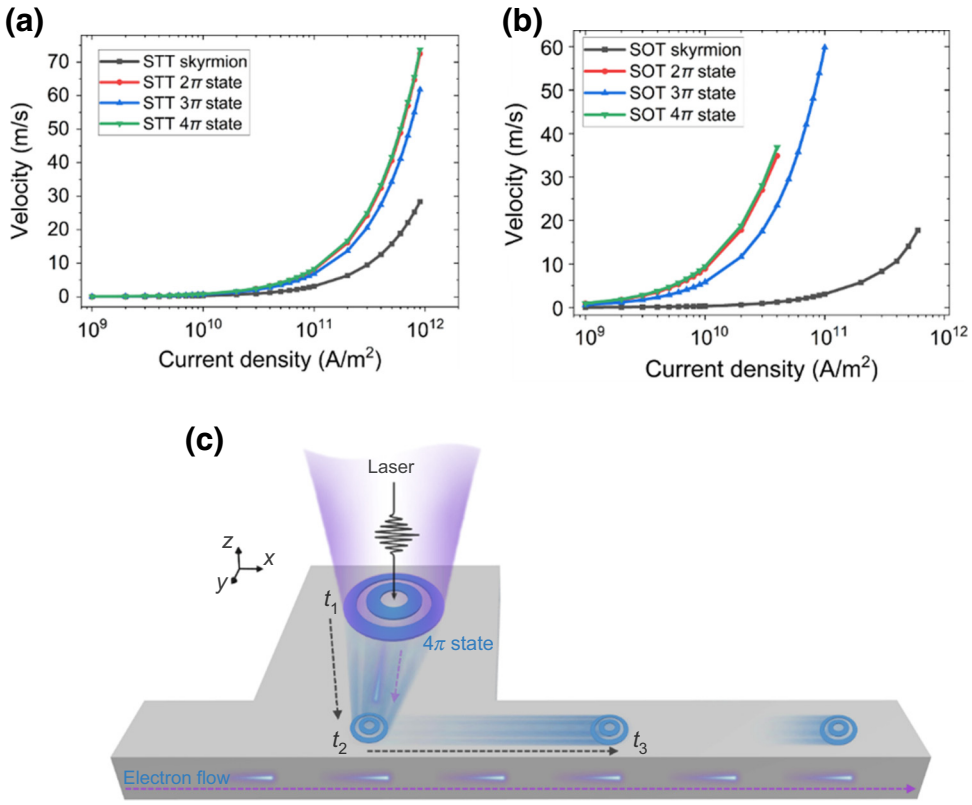

FIG. 5. Current-induced motion of 4π QP. Velocity of the generated magnetic quasiparticles with current in STT (a) or SOT (b) geometry. (c) Schematic diagram of a racetrack memory prototype system working with 4π QP.

subjected to STTs and SOTs. STTs can be decomposed into adiabatic and nonadiabatic components, the expressions of which are provided in previous works [35,47]:

$$\tau_{\mathrm{STT_adiabatic}} = \frac{u}{M_s{}^2}\left(\mathbf{M}\times\frac{\partial\mathbf{M}}{\partial x}\times\mathbf{M}\right), \tag{5}$$

$$\tau_{\mathrm{STT_nonadiabatic}} = -\frac{\beta u}{M_s}\left(\mathbf{M}\times\frac{\partial\mathrm{M}}{\partial x}\right), \tag{6}$$

with $u=\gamma_g(\hbar jP/2eM_s)$. Here, j is the current density in A/m^2, P is the unitless spin polarization, e is the electron charge, and β is the nonadiabaticity factor. The direction of electron flow is along $+x$. In our simulations, we used the values $P=0.4$ and $\beta=0.2$ [47]. Similarly, SOTs can be split into adiabatic and nonadiabatic components, whose expressions are [35,47]:

$$\tau_{\mathrm{SOT_adiabatic}} = \frac{u_{\mathrm{SOT}}}{M_s{}^2 d}\,(\mathbf{M}\times\sigma\times\mathbf{M}), \tag{7}$$

$$\tau_{\mathrm{SOT_nonadiabatic}} = \frac{\beta_{\mathrm{SOT}}u_{\mathrm{SOT}}}{M_s d}(\mathbf{M}\times\sigma), \tag{8}$$

with $u_{\mathrm{SOT}}=\gamma_g(\hbar j\alpha_H/2eM_s)$; d denotes the film thickness in meters, β_{SOT} denotes the unitless nonadiabaticity factor associated with SOT, α_H denotes the unitless current conversion factor, and σ is the current-polarization unit vector along $-y$. We assumed $\alpha_H=0.15$ and $\beta_{\mathrm{SOT}}=-2$ [47]. We chose a ferromagnetic thickness of $d=1\times10^{-9}$ m, consistent with experimental reports [51].

By applying STT or SOT to the four types of quasiparticles, we calculated their longitudinal velocities for various current densities, as shown in Figs. 5(a) and 5(b). We observed that, for both excitation types, the 4π QP exhibits the fastest quasiparticle velocity, followed by the 2π QP, the 3π QP, and finally the skyrmion. The lower velocity of odd n values compared to their even counterparts is due to the skyrmion Hall effect, which generates a side contribution to the velocity with a resulting loss of longitudinal velocity [35]. Odd n values have a topological charge of $Q=1$, while even n values have a zero topological charge, and therefore, do not exhibit skyrmion Hall effects. The impact of Q on the motion of the quasiparticle can be observed by comparing Videos 1 and 2, which, respectively, show the motion of a skyrmion and a 2π QP when applying STT with a current density of 5.10^{11} A/m^2. Concerning quasiparticles with a nonzero topological charge, the dependence of the skyrmion Hall angle on the current density is shown in Fig. S9 within the Supplemental Material [42] for both π QP and 3π QP. Additionally, Figs. 5(a) and 5(b) have more points for the skyrmion state than for the other states, since the other states are not stable for high current densities. Moreover, it appears that, as

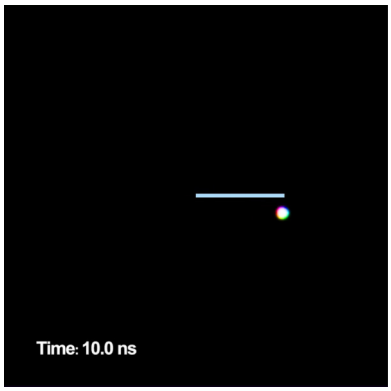

VIDEO 1. Motion of skyrmion (π QP) when applying STT with a current density of 5.10^{11} A/m^2 (blue line is a reference line).

n increases, the stability of the quasiparticle with respect to current decreases, i.e., a lower threshold value of the current density breaks the magnetic order.

IV. DISCUSSION

As previously demonstrated, a 2π QP exhibits a greater velocity than a skyrmion owing to its absence of topological charge. In our current study, however, we not only establish the existence of stable states for higher values of n, but also reveal that even $n\pi$ QPs exhibit higher velocities for larger n values. This discovery offers an alternative avenue for exploring material parameters that could facilitate the stabilization of even $n\pi$ QPs. In addition to their stability, temporary $n\pi$ QPs with higher values could also be generated in materials with lower damping. As Fig. 3(b) illustrates, light-induced polarized magnetic fields are promising candidates for the generation of $n\pi$ QPs, given the large diameter of the beam and the empty center, which allows for the creation of small concentric rings. It is worth noting that $n\pi$ QPs with n values higher than four have been demonstrated previously, but only in materials that are shaped in a circular manner to stabilize the $n\pi$ QP [35]. In our work, the creation of the $n\pi$ QP does not depend on the material shape but is inherited from the light-polarization geometry.

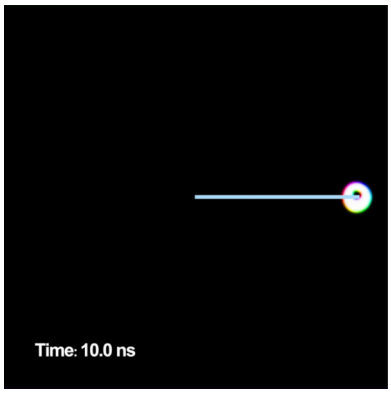

VIDEO 2. Motion of 2π QP when applying STT with a current density of 5.10^{11} A/m^2 (blue line is a reference line).

Finally, a schematic diagram of a racetrack memory prototype system working with a 4π QP is proposed, as depicted in Fig. 5(c). The working principle of such a racetrack can be divided into several stages. First, a 4π QP is generated during the laser pulse that lasts until t_1. Here, only half of the tightly focused 4π configuration is shown. Because the size of the quasiparticle created is similar to the beam size at t_1, it is not generated on the main path of the racetrack, but rather on a pad located on the side of the track. As illustrated in Fig. 4, it takes 1.2×10^{-8} s for the quasiparticle to reach its equilibrium state in the absence of external perturbation. The quasiparticle can then be transported to the main track using a STT current pulse. To save time, STT can be applied while the quasiparticle size is still decreasing. Our observations in Fig. S10 within the Supplemental Material [42] demonstrate that the quasiparticle retains its integrity when STT is applied with a current density of $j = 1.10 \times 10^{11}$ A/m^2 only 1 ps after t_1, the end of the laser pulse. Furthermore, the relaxation time and the final diameter of the 4π QP are not affected by the STT. In our geometry, we consider a pad with dimensions of 1024×1024 nm^2 and a racetrack lateral size of 200 nm. Therefore, it takes 1.5×10^{-8} s for the quasiparticle to reach the main body of the racetrack at t_2. From t_2 to t_3, the quasiparticle behaves as it would on a standard racetrack memory device, moving with the chosen spin torque. The main advantage of the racetrack geometry we propose is that it combines accessible sizes of laser beams and faster topological quasiparticles than conventional skyrmions. While we propose a racetrack memory based on STT, SOT could also be used, but its operation frequency would be more limited due to the lower maximum velocity observed in Fig. 5(b).

V. CONCLUSION

Our study has revealed the potential of using a unique RPMF distribution to produce topological spin textures with varying sizes and properties. Notably, by leveraging laser beams of readily accessible dimensions, we were able to generate quasiparticles with significantly reduced dimensions, thanks to the size-reducing mechanism that occurred upon their formation. Through manipulation of the RPMF amplitude or material parameters, stable states with higher values of n, including even $n\pi$ quasiparticles, can be created and stabilized, thereby opening up avenues for research into material parameters that can support these quasiparticles. Of crucial importance is the relaxation mechanism of the generated spin texture at the center of the beam, given that the RPMF has a null magnitude at this location. Moreover, while quasiparticles can

be displaced using STT and SOT, the 4π quasiparticle stands out as the fastest and most-promising candidate for integration into racetrack memories.

ACKNOWLEDGMENTS

The authors thank Stéphane Mangin for valuable discussions. The authors are grateful for financial support from the National Key R&D Program of China (Grant No. 2023YFF0719200), the National Natural Science Foundation of China (Grants No. 12250410245 and No. 12004025), and the Beihang Hefei Innovation Research Institute Project (Grant No. BHKX-19-01).

The authors declare that there are no conflicts of interest related to this article.

[1] Q. Shao, Skyrmions get pushed beyond the limit, Nat. Electron. **3**, 16 (2020).

[2] A. Fert, N. Reyren, and V. Cros, Magnetic skyrmions: Advances in physics and potential applications, Nat. Rev. Mater. **2**, 17031 (2017).

[3] A. Fert, V. Cros, and J. Sampaio, Skyrmions on the track, Nat. Nanotechnol. **8**, 152 (2013).

[4] N. Nagaosa and Y. Tokura, Topological properties and dynamics of magnetic skyrmions, Nat. Nanotechnol. **8**, 899 (2013).

[5] I. M. Alliati, R. F. L. Evans, K. S. Novoselov, and E. J. G. Santos, Relativistic domain-wall dynamics in van der Waals antiferromagnet $MnPS_3$, npj Comput. Mater. **8**, 3 (2022).

[6] D. Abdul-Wahab, E. Iacocca, R. F. L. Evans, A. Bedoya-Pinto, S. Parkin, K. S. Novoselov, and E. J. G. Santos, Domain wall dynamics in two-dimensional van der Waals ferromagnets, Appl. Phys. Rev. **8**, 041411 (2021).

[7] K. Taguchi, J. Ohe, and G. Tatara, Ultrafast magnetic vortex core switching driven by the topological inverse Faraday effect, Phys. Rev. Lett. **109**, 127204 (2012).

[8] Y. S. Liu, H. Y. Cheng, Y. Xu, P. Vallobra, S. Eimer, X. Q. Zhang, X. J. Wu, T. X. Nie, and W. S. Zhao, Separation of emission mechanisms in spintronic terahertz emitters, Phys. Rev. B **104**, 064419 (2021).

[9] Y. Jiang, X. Zhang, Y. Liu, P. Vallobra, S. Eimer, F. Zhang, Y. Du, F. Liu, Y. Xu, and W. Zhao, Spintronic terahertz emitter with integrated electromagnetic control, Chin. Opt. Lett. **20**, 043201 (2022).

[10] S. C. Wang, C. Wei, Y. H. Feng, H. K. Cao, W. Z. Li, Y. Y. Cao, B. O. Guan, A. Tsukamoto, A. Kirilyuk, A. V. Kimel, *et al.*, Dual-shot dynamics and ultimate frequency of all-optical magnetic recording on GdFeCo, Light: Sci. Appl. **10**, 8 (2021).

[11] A. V. Kimel and M. Li, Writing magnetic memory with ultrashort light pulses, Nat. Rev. Mater. **4**, 189 (2019).

[12] J. W. Liao, P. Vallobra, L. O'Brien, U. Atxitia, V. Raposo, D. Petit, T. Vemulkar, G. Malinowski, M. Hehn, E. Martinez, *et al.*, Controlling all-optical helicity-dependent switching in engineered rare-earth free synthetic ferrimagnets, Adv. Sci. (Weinh.) **6**, 1901876 (2019).

[13] P. Vallobra, T. Fache, Y. Xu, L. Zhang, G. Malinowski, M. Hehn, J. C. Rojas-Sánchez, E. E. Fullerton, and S. Mangin, Manipulating exchange bias using all-optical helicity-dependent switching, Phys. Rev. B **96**, 144403 (2017).

[14] M. Strungaru, M. Augustin, and E. J. G. Santos, Ultrafast laser-driven topological spin textures on a 2D magnet, npj Comput. Mater. **8**, 169 (2022).

[15] M. Finazzi, M. Savoini, A. R. Khorsand, A. Tsukamoto, A. Itoh, L. Duo, A. Kirilyuk, T. Rasing, and M. Ezawa, Laser-induced magnetic nanostructures with tunable topological properties, Phys. Rev. Lett. **110**, 177205 (2013).

[16] G. Berruto, I. Madan, Y. Murooka, G. M. Vanacore, E. Pomarico, J. Rajeswari, R. Lamb, P. Huang, A. J. Kruchkov, Y. Togawa, *et al.*, Laser-induced skyrmion writing and erasing in an ultrafast cryo-Lorentz transmission electron microscope, Phys. Rev. Lett. **120**, 117201 (2018).

[17] S. G. Je, P. Vallobra, T. Srivastava, J. C. Rojas-Sanchez, T. H. Pham, M. Hehn, G. Malinowski, C. Baraduc, S. Auffret, G. Gaudin, *et al.*, Creation of magnetic skyrmion bubble lattices by ultrafast laser in ultrathin films, Nano Lett. **18**, 7362 (2018).

[18] K. Gerlinger, B. Pfau, F. Büttner, M. Schneider, L.-M. Kern, J. Fuchs, D. Engel, C. M. Günther, M. Huang, I. Lemesh, *et al.*, Application concepts for ultrafast laser-induced skyrmion creation and annihilation, Appl. Phys. Lett. **118**, 192403 (2021).

[19] R. Juge, N. Sisodia, J. U. Larranaga, Q. Zhang, V. T. Pham, K. G. Rana, B. Sarpi, N. Mille, S. Stanescu, R. Belkhou, *et al.*, Skyrmions in synthetic antiferromagnets and their nucleation via electrical current and ultra-fast laser illumination, Nat. Commun. **13**, 4807 (2022).

[20] H. Fujita and M. Sato, Ultrafast generation of skyrmionic defects with vortex beams: Printing laser profiles on magnets, Phys. Rev. B **95**, 054421 (2017).

[21] X. Zhang, G. Rui, Y. Xu, F. Zhang, Y. Du, M. Lian, A. Wang, H. Ming, and W. Zhao, Tailoring the magnetic field induced by the first higher order mode of an optical fiber, Opt. Express **28**, 2572 (2020).

[22] L. E. Helseth, Light-induced magnetic vortices, Opt. Lett. **36**, 987 (2011).

[23] G. M. Choi, J. H. Oh, D. K. Lee, S. W. Lee, K. W. Kim, M. Lim, B. C. Min, K. J. Lee, and H. W. Lee, Optical spin-orbit torque in heavy metal-ferromagnet heterostructures, Nat. Commun. **11**, 1482 (2020).

[24] C. Wan, Q. Cao, J. Chen, A. Chong, and Q. Zhan, Toroidal vortices of light, Nat. Photonics **16**, 519 (2022).

[25] C. Wan, Y. Shen, A. Chong, and Q. Zhan, Scalar optical hopfions, eLight **2**, 22 (2022).

[26] X. Zhang, G. Rui, Y. Xu, F. Zhang, Y. Du, X. Lin, A. Wang, and W. Zhao, Fully controllable three-dimensional light-induced longitudinal magnetization using a single objective lens, Opt. Lett. **45**, 2395 (2020).

[27] X. Zhang, F. Liu, Y. Jiang, Y. Xu, X. Lin, G. Rui, M. Bai, A. Wang, D. Zhu, and W. Zhao, Controlled light-induced longitudinal magnetization spots with opposite directions, J. Opt. **23**, 095401 (2021).

[28] M. Lin, W. Zhang, C. Liu, L. Du, and X. Yuan, Photonic spin skyrmion with dynamic position control, ACS Photonics **8**, 2567 (2021).

[29] X. Zhang, Y. Jiang, Y. Xu, G. Rui, X. Lin, A. Wang, M. Bai, W. Zhao, and D. Zhu, Light-induced radially polarized magnetic fields, Opt. Commun. **491**, 126975 (2021).
[30] Q. Zhan, Cylindrical vector beams: From mathematical concepts to applications, Adv. Opt. Photonics **1**, 1 (2009).
[31] R. Chen, J. Wang, X. Zhang, A. Wang, H. Ming, F. Li, D. Chung, and Q. Zhan, High efficiency all-fiber cylindrical vector beam laser using a long-period fiber grating, Opt. Lett. **43**, 755 (2018).
[32] K. Litzius, I. Lemesh, B. Krüger, P. Bassirian, L. Caretta, K. Richter, F. Büttner, K. Sato, O. A. Tretiakov, J. Förster, *et al.*, Skyrmion Hall effect revealed by direct time-resolved x-ray microscopy, Nat. Phys. **13**, 170 (2016).
[33] W. Jiang, X. Zhang, G. Yu, W. Zhang, X. Wang, M. Benjamin Jungfleisch, John E. Pearson, X. Cheng, O. Heinonen, K. L. Wang, *et al.*, Direct observation of the skyrmion Hall effect, Nat. Phys. **13**, 162 (2017).
[34] X. Zhang, Y. Zhou, and M. Ezawa, Magnetic bilayer-skyrmions without skyrmion Hall effect, Nat. Commun. **7**, 10293 (2016).
[35] X. Zhang, J. Xia, Y. Zhou, D. Wang, X. Liu, W. Zhao, and M. Ezawa, Control and manipulation of a magnetic skyrmionium in nanostructures, Phys. Rev. B **94**, 094420 (2016).
[36] B. Gobel, A. F. Schaffer, J. Berakdar, I. Mertig, and S. S. P. Parkin, Electrical writing, deleting, reading, and moving of magnetic skyrmioniums in a racetrack device, Sci. Rep. **9**, 12119 (2019).
[37] L. Shen, X. Li, Y. Zhao, J. Xia, G. Zhao, and Y. Zhou, Current-induced dynamics of the antiferromagnetic skyrmion and skyrmionium, Phys. Rev. Appl. **12**, 064033 (2019).
[38] M. Miyata, J.-i. Ohe, and G. Tatara, Topological charge control of skyrmion structure in frustrated magnets by circularly polarized light, Phys. Rev. Appl. **18**, 014075 (2022).
[39] Y. Chen, Y. He, L. Liu, Z. Tian, and J. Dai, Interaction of colliding laser pulses with gas plasma for broadband coherent terahertz wave generation, Photonics Res. **11**, 1562 (2023).
[40] Q. Zhan and J. Leger, Focus shaping using cylindrical vector beams, Opt Express **10**, 324 (2002).
[41] X. Zhang, G. Rui, Y. Xu, F. Zhang, Y. Du, M. Lian, X. Lin, A. Wang, H. Ming, and W. Zhao, Multi-layer magnetic recording driven by a tunable laser, Chin. Opt. Lett. **18**, 102501 (2020).
[42] See the Supplemental Material at http://link.aps.org/supplemental/10.1103/PhysRevApplied.21.044041 for the total electric field on the focal plane; the normalized radial distribution function, $b(r)$, of the two CVBs; evolution of magnetization from the end of the pulse for $I_0=4$; change of the topological charge as a function of time; evolution of magnetization during the pulse for $I_0=10$ with only RPMF; different magnetization state at the end of the pulse for $I_0=20$; reduction to a 4π QP from a 9π QP; reduction to a 3π QP with a different exchange coupling; skyrmion Hall effect characteristics for different $n\pi$ QP; and generation and motion of 4π QP during its relaxation.
[43] K. Vahaplar, A. M. Kalashnikova, A. V. Kimel, S. Gerlach, D. Hinzke, U. Nowak, R. Chantrell, A. Tsukamoto, A. Itoh, A. Kirilyuk, *et al.*, All-optical magnetization reversal by circularly polarized laser pulses: Experiment and multiscale modeling, Phys. Rev. B **85**, 104402 (2012).
[44] G. M. Choi, A. Schleife, and D. G. Cahill, Optical-helicity-driven magnetization dynamics in metallic ferromagnets, Nat. Commun. **8**, 15085 (2017).
[45] T. D. Cornelissen, R. Córdoba, and B. Koopmans, Microscopic model for all optical switching in ferromagnets, Appl. Phys. Lett. **108**, 142405 (2016).
[46] M. Ezawa, Giant skyrmions stabilized by dipole-dipole interactions in thin ferromagnetic films, Phys. Rev. Lett. **105**, 197202 (2010).
[47] J. Sampaio, V. Cros, S. Rohart, A. Thiaville, and A. Fert, Nucleation, stability and current-induced motion of isolated magnetic skyrmions in nanostructures, Nat. Nanotechnol. **8**, 839 (2013).
[48] D. Cortés-Ortuño, M. Beg, V. Nehruji, L. Breth, R. Pepper, T. Kluyver, G. Downing, T. Hesjedal, P. Hatton, T. Lancaster, *et al.*, Proposal for a micromagnetic standard problem for materials with Dzyaloshinskii–Moriya interaction, New J. Phys. **20**, 113015 (2018).
[49] W. Zhang, T. X. Huang, M. Hehn, G. Malinowski, M. Verges, J. Hohlfeld, Q. Remy, D. Lacour, X. R. Wang, G. P. Zhao, *et al.*, Optical creation of skyrmions by spin reorientation transition in ferrimagnetic CoHo alloys, ACS Appl. Mater. Interfaces **15**, 5608 (2023).
[50] J. J. Joos, P. Bassirian, P. Gypens, J. Mulkers, K. Litzius, B. Van Waeyenberge, and J. Leliaert, Tutorial: Simulating modern magnetic material systems in MUMAX3, J. Appl. Phys. **134**, 171101 (2023).
[51] M. Bersweiler, K. Dumesnil, D. Lacour, and M. Hehn, Impact of buffer layer and Pt thickness on the interface structure and magnetic properties in (Co/Pt) multilayers, J. Phys.: Condens.Matter **28**, 336005 (2016).